Optical Phase Noise Cancellation through Differential Detection Using Analog Circuit Techniques

Toshiyuki Inoue[1]*, Yuta Hanai[2], Itsuki Tanaka[2], Daisuke Ito[3], and Makoto Nakamura[3]
[1]*Kyoto Institute of Technology*, Matsugasaki, Sakyo-ku, Kyoto 606-8585, Japan
inoue@vlsi.es.kit.ac.jp *Corresponding author
[2]*The University of Shiga Prefecture*, 2500 Hassaka, Hikone, Shiga 522-8533, Japan
[3]*Gifu University*, 1-1 Yanagido, Gifu 501-1193, Japan

***Abstract*—In optical fiber communication systems, intensity modulation and direct detection (IM-DD) is widely used. In contrast, coherent detection based on optical phase modulation improves receiver sensitivity compared to IM-DD. This paper describes a method for canceling optical phase noise through differential detection. This method is particularly suitable for optical fiber networks requiring high reliability, such as in-vehicle optical fiber networks. First, the principle of noise cancellation is explained, and its effectiveness is verified through theoretical analysis considering the frequency bandwidth of the analog circuits. Furthermore, the post-layout simulation results of the designed analog circuits in a 65-nm CMOS process demonstrate effective noise-canceling performance at 25 Gb/s.**

***Index Terms*—Coherent optical fiber communication, 65-nm CMOS, Fully autonomous driving system.**

I. Introduction

Optical fiber communication technique has been mainly applied to a backbone optical network and fiber to the home (FTTH) [1], and it enables the transfer of big data gathered by various terminals, such as smart phones and wireless sensors. In recent years, data center interconnection (DCI) application is a hot topic of optical fiber communication technique because the amount of data traffic in a data center has increased explosively [2]. Because a data-transfer system for DCI requires higher speed and larger capacity, the length of electrical wiring should be shortened and an electrical network should be replaced with an optical network. One of the key techniques for DCI is the co-packaged optics (CPO) technique, in which optical transceivers and a switch ASIC are integrated into the same package [3], [4].

In optical fiber communication systems, the intensity modulation and direct detection (IM-DD) method is the mainstream method due to a simple configuration. In contrast, the coherent detection method based on optical phase modulation improves receiver sensitivity and bit-error rate (BER) compared to IM-DD method. The coherent detection method has been proposed and developed since the 1980s [5], and the digital coherent technique using analog-to-digital converters (ADCs) and digital signal processors (DSPs) had taken place of the earlier analog coherent technique [6]. However, the DSP-free analog coherent method has drawn renewed attention for DCI application because ADCs and DSPs consume large amounts of power [7]–[11].

These research results were obtained from the commissioned research (No. 23701) by National Institute of Information and Communications Technology (NICT, PO: Ryo Takahashi), Japan.

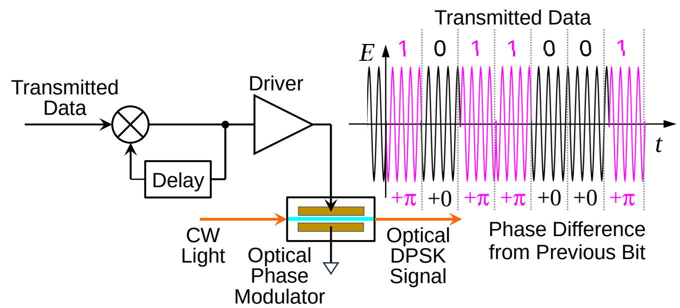

Fig. 1. Method for optical DPSK modulation.

In this paper, an analog coherent method for canceling optical phase noise through differential detection is presented. This method is particularly suitable for high-reliability optical fiber networks, such as in-vehicle optical fiber networks. First, the principle of demodulating optical DPSK signal, which is one of the phase-modulation signal, and canceling optical phase noise is explained. Next, based on theoretical equations, the noise-canceling effect is verified, and its tolerance for variation of operating conditions is evaluated. Then, the post-layout simulation (PLS) results of the designed analog circuits using the parameters of the 65-nm CMOS process are shown, and the noise-canceling performance is demonstrated at 25 Gb/s.

II. Demodulation of Optical DPSK Signal and Canceling Optical Phase Noise

In this section, a method for demodulating an optical DPSK signal is presented. Also, an operation principle of canceling optical phase noise is described.

A. Optical DPSK modulation

Fig. 1 shows a block diagram for the optical DPSK modulation and a waveform of an optical DPSK signal. A continuous -wave (CW) light from a laser diode is modulated by an optical phase modulator. A DPSK pattern is generated by a frequency mixer (or exclusive OR circuit) and a delay element (delay line or delay flip-flop circuit) and is input to an optical phase modulator through a modulator driver. As a result, the

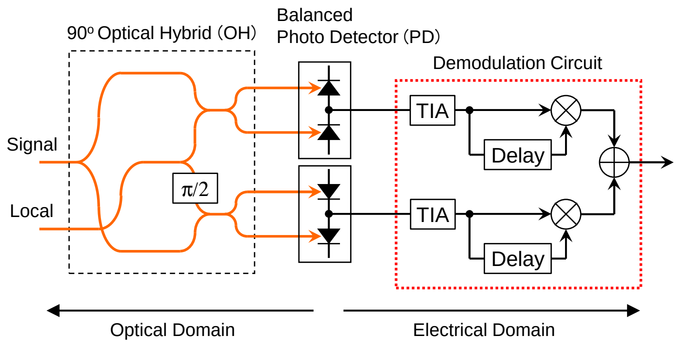

Fig. 2. Block diagram of optical DPSK signal receiver.

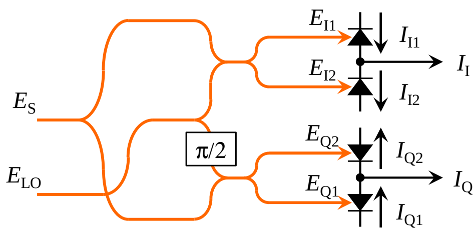

Fig. 3. Block diagram of optical to electrical signal conversion.

optical phase difference between the present and previous bits becomes 0 or π (applied voltage: 0–V_π) corresponding to the transmitted data of '0' or '1', respectively.

B. Operation principle of demodulation of DPSK signal using differential detection

A block diagram of an optical DPSK signal receiver is shown in Fig. 2. It consists of a 90-degree optical hybrid (90° OH) using optical 3-dB couplers and a 90-degree optical phase shifter, balanced photodetectors (PDs), and a demodulation circuit. Fig. 3 shows a block diagram of the optical to electrical signal conversion. When the complex amplitude, the angular frequency, and time-varying phase of the signal light are put as A_{S}, ω_{S}, $\theta_{\mathrm{S}}(t)$, respectively, the complex electric field $E_{\mathrm{S}}(t)$is given by

$$E_{\mathrm{S}}(t) = A_{\mathrm{S}} \exp[j\{\omega_{\mathrm{S}} t + \theta_{\mathrm{S}}(t)\}], \tag{1}$$

In the same manner, the complex electric field of the local light (LO)is given by

$$E_{\mathrm{LO}}(t) = A_{\mathrm{LO}} \exp[j\{\omega_{\mathrm{LO}} t + \theta_{\mathrm{LO}}(t)\}], \tag{2}$$

where A_{LO}, ω_{LO}, $\theta_{\mathrm{LO}}(t)$ are the complex amplitude, the angular frequency, and the time-varying phase of LO light, respectively. In the following explanation, (t) is omitted for simplicity. The optical power P is related to the complex electric field E as

$$P = k|E|^2, \tag{3}$$

where k is the constant of proportionality. After the signal and local lights pass through the 90° OH, we can obtain the four outputs as

$$E_{\mathrm{I1}} = \frac{1}{2}(E_{\mathrm{S}} + E_{\mathrm{LO}}), \tag{4}$$

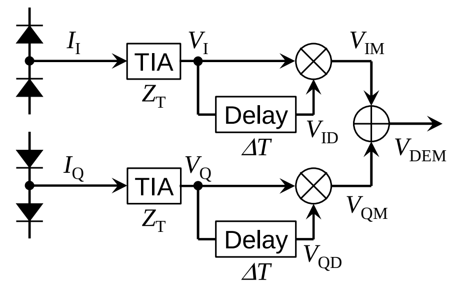

Fig. 4. Block diagram of demodulation circuit for optical DPSK signal.

$$E_{\mathrm{I2}} = \frac{1}{2}(E_{\mathrm{S}} - E_{\mathrm{LO}}), \tag{5}$$

$$E_{\mathrm{Q1}} = \frac{1}{2}(E_{\mathrm{S}} + jE_{\mathrm{LO}}), \tag{6}$$

$$E_{\mathrm{Q2}} = \frac{1}{2}(E_{\mathrm{S}} - jE_{\mathrm{LO}}). \tag{7}$$

Here, subscripts I and Q mean in- and quadrature-phase signals, respectively. Using Eq. (3), the output currents from each PD can be expressed as

$$\begin{aligned} I_{\mathrm{I1}} &= RP_{\mathrm{I1}} \\ &= kR|E_{\mathrm{I1}}|^2 \\ &= \frac{kR}{4}\left[|E_{\mathrm{S}}|^2 + |E_{\mathrm{LO}}|^2 + 2\mathrm{Re}\left\{E_{\mathrm{S}}E_{\mathrm{LO}}^*\right\}\right], \end{aligned} \tag{8}$$

$$\begin{aligned} I_{\mathrm{I2}} &= RP_{\mathrm{I2}} \\ &= kR|E_{\mathrm{I2}}|^2 \\ &= \frac{kR}{4}\left[|E_{\mathrm{S}}|^2 + |E_{\mathrm{LO}}|^2 - 2\mathrm{Re}\left\{E_{\mathrm{S}}E_{\mathrm{LO}}^*\right\}\right], \end{aligned} \tag{9}$$

$$\begin{aligned} I_{\mathrm{Q1}} &= RP_{\mathrm{Q1}} \\ &= kR|E_{\mathrm{Q1}}|^2 \\ &= \frac{kR}{4}\left[|E_{\mathrm{S}}|^2 + |E_{\mathrm{LO}}|^2 + 2\mathrm{Im}\left\{E_{\mathrm{S}}E_{\mathrm{LO}}^*\right\}\right], \end{aligned} \tag{10}$$

$$\begin{aligned} I_{\mathrm{Q2}} &= RP_{\mathrm{Q2}} \\ &= kR|E_{\mathrm{Q2}}|^2 \\ &= \frac{kR}{4}\left[|E_{\mathrm{S}}|^2 + |E_{\mathrm{LO}}|^2 - 2\mathrm{Im}\left\{E_{\mathrm{S}}E_{\mathrm{LO}}^*\right\}\right], \end{aligned} \tag{11}$$

where R is the responsivity of the PD. Then, the balanced PD outputs I_1 and I_2 can be obtained from

$$\begin{aligned} I_{\mathrm{I}} &= I_{\mathrm{I1}} - I_{\mathrm{I2}} \\ &= kR \cdot \mathrm{Re}\{E_{\mathrm{S}}E_{\mathrm{LO}}^*\} \\ &= I' \cos[(\omega_{\mathrm{S}} - \omega_{\mathrm{LO}})t + (\theta_{\mathrm{S}} - \theta_{\mathrm{LO}})], \end{aligned} \tag{12}$$

$$\begin{aligned} I_{\mathrm{Q}} &= I_{\mathrm{Q1}} - I_{\mathrm{Q2}} \\ &= kR \cdot \mathrm{Im}\{E_{\mathrm{S}}E_{\mathrm{LO}}^*\} \\ &= I' \sin[(\omega_{\mathrm{S}} - \omega_{\mathrm{LO}})t + (\theta_{\mathrm{S}} - \theta_{\mathrm{LO}})], \end{aligned} \tag{13}$$

where $kRA_{\mathrm{S}}A_{\mathrm{LO}}^*$ is replaced with I'. Assuming the homodyne detection ($\omega_{\mathrm{S}} = \omega_{\mathrm{LO}}$), Eqs. (12) and (13) can be simplified as

$$I_{\mathrm{I}} = I' \cos(\theta_{\mathrm{S}} - \theta_{\mathrm{LO}}), \tag{14}$$

$$I_{\mathrm{Q}} = I' \sin(\theta_{\mathrm{S}} - \theta_{\mathrm{LO}}). \tag{15}$$

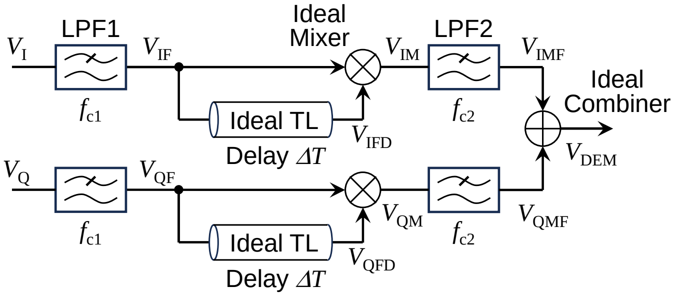

Fig. 5. Block diagram of equivalent model for demodulation circuit.

Next, we consider the phase change due to the phase modulation and the phase noise. We put the time-varying phase of the signal and LO lights as $\theta_{\mathrm{S}}(t) = \theta_{\mathrm{S0}} + \alpha(t)$ and $\theta_{\mathrm{LO}}(t) = \theta_{\mathrm{LO0}} + \beta(t)$, where θ_{S0} and θ_{LO0} are the initial phase of the signal and LO lights, respectively, $\alpha(t)$ is the phase modulation component, and $\beta(t)$ is the phase noise component derived from the noise voltage applying to an optical phase modulator. Fig. 4 shows a block diagram of the demodulation circuit. When the transimpedance gain of each TIA is Z_{T}, the output voltage is calculated as

$$\begin{aligned} V_{\mathrm{I}} &= Z_{\mathrm{T}} I_{\mathrm{I}} \\ &= V' \cos\{\theta_{\mathrm{init}} + \alpha(t) - \beta(t)\}, \end{aligned} \tag{16}$$

$$\begin{aligned} V_{\mathrm{Q}} &= Z_{\mathrm{T}} I_{\mathrm{Q}} \\ &= V' \sin\{\theta_{\mathrm{init}} + \alpha(t) - \beta(t)\}, \end{aligned} \tag{17}$$

where $Z_{\mathrm{T}} I'$ and $\theta_{\mathrm{S0}} - \theta_{\mathrm{LO0}}$ are replaced with V' and θ_{init}, respectively. V_{ID}, V_{QD} are generated by delaying V_{I} and V_{Q} by 1-bit width (ΔT) and can be expressed as

$$V_{\mathrm{ID}} = V' \cos\{\theta_{\mathrm{init}} + \alpha(t - \Delta T) - \beta(t - \Delta T)\}, \tag{18}$$

$$V_{\mathrm{QD}} = V' \sin\{\theta_{\mathrm{init}} + \alpha(t - \Delta T) - \beta(t - \Delta T)\}. \tag{19}$$

When the pairs of V_{I}, V_{ID} and V_{Q}, V_{QD} are input to multipliers (frequency mixers) with the conversion gain of G_{M}, the mixer output V_{IM} and V_{QM} can be obtained from

$$\begin{aligned} V_{\mathrm{IM}} &= G_{\mathrm{M}} V_{\mathrm{I}} V_{\mathrm{ID}} \\ &= G_{\mathrm{M}} V'^2 \cos\{\theta_{\mathrm{init}} + \alpha(t) - \beta(t)\} \\ &\quad \cdot \cos\{\theta_{\mathrm{init}} + \alpha(t - \Delta T) - \beta(t - \Delta T)\}, \end{aligned} \tag{20}$$

$$\begin{aligned} V_{\mathrm{QM}} &= G_{\mathrm{M}} V_{\mathrm{Q}} V_{\mathrm{QD}} \\ &= G_{\mathrm{M}} V'^2 \sin\{\theta_{\mathrm{init}} + \alpha(t) - \beta(t)\} \\ &\quad \cdot \sin\{\theta_{\mathrm{init}} + \alpha(t - \Delta T) - \beta(t - \Delta T)\}. \end{aligned} \tag{21}$$

Note that we assume an operation of the mixer is equivalent to a mathematical multiplication and neglect limitation of the frequency bandwidth. V_{DEM} is the sum of V_{IM} and V_{QM}, and can be obtained from

$$\begin{aligned} V_{\mathrm{DEM}} &= V_{\mathrm{IM}} + V_{\mathrm{QM}} \\ &= V_{\mathrm{G}} \cos\left[\{\alpha(t) - \alpha(t - \Delta T)\}\right. \\ &\qquad \left. - \{\beta(t) - \beta(t - \Delta T)\}\right], \end{aligned} \tag{22}$$

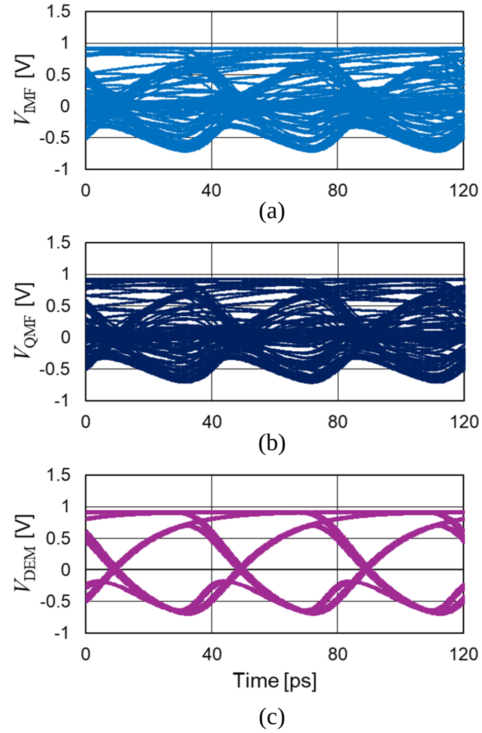

Fig. 6. Eye diagrams of (a) I-signal mixer output V_{IMF}, (b) Q-signal mixer output V_{QMF}, and (c) combiner output V_{DEM} (BR = 25 Gb/s, ΔT = 40 ps, f_{n} = 1 GHz, $\beta_{\mathrm{amp}} = \pi/4$, f_{c1} = 20 GHz, f_{c2} = 12.5 GHz).

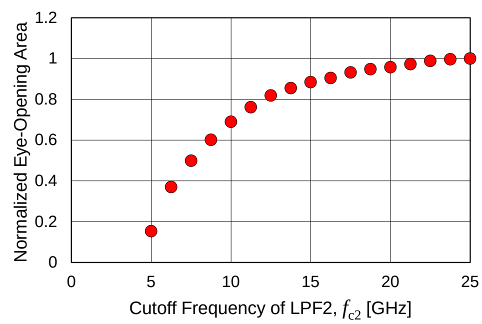

Fig. 7. Dependence of normalized eye-opening area upon cutoff frequency f_{c2} (BR = 25 Gb/s, ΔT = 40 ps, f_{n} = 1 GHz, $\beta_{\mathrm{amp}} = \pi/4$, f_{c1} = 20 GHz).

where $G_{\mathrm{M}} V'^2$ is replaced with V_{G}. Therefore, when the phase change derived from the phase noise is relatively slower compared to the phase modulation ($\beta(t) \cong \beta(t - \Delta T)$), the phase noise can be cancelled out. Consequently, V_{DEM} can be rewritten by

$$V_{\mathrm{DEM}} \cong V_{\mathrm{G}} \cos\{\alpha(t) - \alpha(t - \Delta T)\}. \tag{23}$$

Eq. (23) means that the logic value corresponding the phase difference between the present and previous bits can be extracted, and that the DPSK signal can be demodulated successfully.

III. Theoretical Prediction of Noise-Canceling Effect

To evaluate the noise-canceling effect, we consider an equivalent model for the demodulation circuit. Fig. 5 shows a

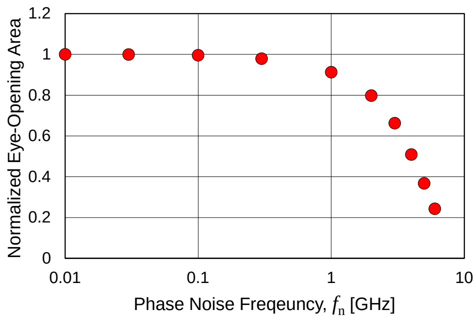

Fig. 8. Dependence of normalized eye-opening area upon noise frequency f_{n} (*BR* $=$ 25 Gb/s, $\Delta T = 40$ ps, $\beta_{\mathrm{amp}} = \pi/4$, $f_{\mathrm{c1}} = f_{\mathrm{c2}} = 20$ GHz).

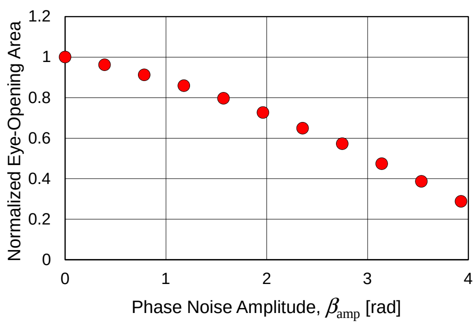

Fig. 9. Dependence of normalized eye-opening area upon noise amplitude β_{amp} (*BR* $=$ 25 Gb/s, $\Delta T = 40$ ps, $f_{\mathrm{n}} = 1$ GHz, $f_{\mathrm{c1}} = f_{\mathrm{c2}} = 20$ GHz).

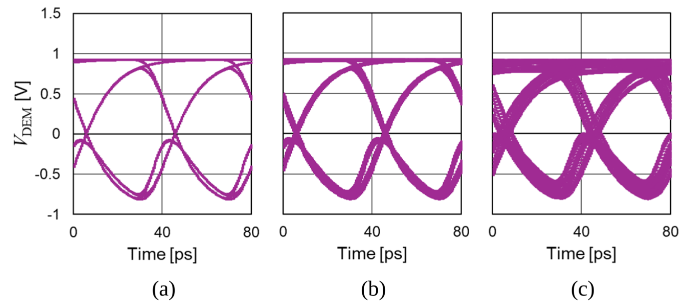

Fig. 10. Eye diagrams of (a) $f_{\mathrm{n}} = 0.1$ GHz, (b) $f_{\mathrm{n}} = 1$ GHz, and (c) $f_{\mathrm{n}} =$ 3 GHz (*BR* $=$ 25 Gb/s, $\Delta T = 40$ ps, $\beta_{\mathrm{amp}} = \pi/4$, $f_{\mathrm{c1}} = f_{\mathrm{c2}} = 20$ GHz).

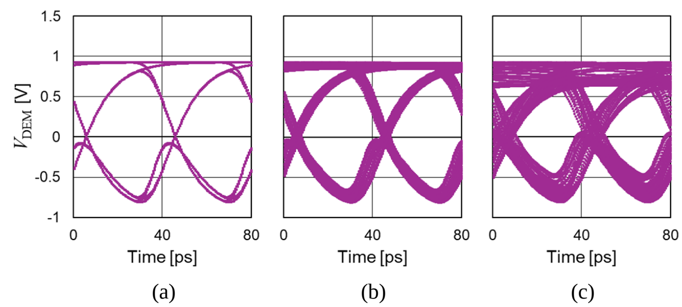

Fig. 11. Eye diagrams of (a) $\beta_{\mathrm{amp}} = 0$, (b) $\beta_{\mathrm{amp}} = \pi/2$, and (c) $\beta_{\mathrm{amp}} = \pi$ (*BR* $=$ 25 Gb/s, $\Delta T = 40$ ps, $f_{\mathrm{n}} = 1$ GHz, $f_{\mathrm{c1}} = f_{\mathrm{c2}} = 20$ GHz).

block diagram of the equivalent model. Based on the mathematical model using Eqs. (16)–(22), the frequency bandwidth is limited by a first-order low-pass filter (LPF) to simulate the actual circuit behavior. The LPF1 has the -3-dB cutoff frequency of f_{c1} and is used to smooth the rising/falling edges of the input signal. The LPF2 has the -3-dB cutoff frequency of f_{c2} and is used to limit the frequency bandwidth of the frequency mixer. Ideal transmission lines (TLs) gives the delay time of ΔT without electrical loss. Operations of ideal mixers and combiners are equivalent to mathematical multiplication and addition, respectively. To quantify the noise-canceling effect, we compare the eye-opening areas (diamond shape) of the demodulation output under each calculation condition. In Eqs. (16) and (17), we define $\beta(t)$ as $\beta_{\mathrm{amp}} \cos(2\pi f_{\mathrm{n}} t)$, where β_{amp} and f_{n} are the phase noise amplitude and frequency, respectively, and express $\alpha(t)$ as a 25-Gb/s NRZ (PRBS 2^9-1) signal with the amplitude from 0 to π. The initial phase θ_{init} is set to $-\pi/4$.

Fig. 6 shows the eye diagrams of (a) I-signal mixer output V_{IMF}, (b) Q-signal mixer output V_{QMF}, and (c) combiner output V_{DEM}. It seems that eye diagrams with various amplitudes are overlaid. This is because $\beta(t)$ changes periodically with the amplitude of β_{amp} and the frequency of f_{n} and the amplitudes of V_{I} and V_{Q} also change. On the other hand, the demodulation output has a clear eye opening because of the noise-canceling effect of Eq. (22). The dependence of the normalized eye-opening area upon the cutoff frequency of LPF2 is shown in Fig. 7, where the values of the vertical axis is normalized by the value at f_{c2} =25 GHz. From Fig. 7, it is desirable that the frequency bandwidth of the mixer is larger than 12.5 GHz for 25-Gb/s data transmission.

Figs. 8 and 9 show the dependencies of the normalized eye-opening area upon the phase noise frequency f_{n} and amplitude β_{amp}, respectively. As the noise frequency increases, the eye-opening area becomes smaller in the range more than 0.1 GHz. This is because the difference between $\beta(t)$ and $\beta(t - \Delta T)$ becomes larger. $\beta_{\mathrm{amp}} = \pi/2$ corresponds to phase noise with peak-to-peak value of π, which means that the half-wave voltage V_π is applied to an optical phase modulator as a noise voltage. The value of V_π depends on the interaction length of the phase modulator, and it is larger than a few volts in the case of a lithium niobate modulator. The eye diagrams for each phase-noise condition are shown in Figs. 10 and 11.

We examined tolerance for variation of the delay time ΔT and the operating bitrate *BR*. Figs. 12 and 13 show the dependencies of the normalized eye-opening area upon ΔT and *BR*, respectively. It is found that the shape of the data series is asymmetrical to the reference condition ($\Delta T = 40$ ps in Fig. 12 and *BR* $= 25$ Gb/s in Fig. 13). When ΔT exceeds the 1-bit width, the phase of the present bit affects not only that of the previous bit but also that of the before previous bit in Eq. (22). Therefore, the delay detection cannot operate properly. For the same reason, the phase of the present bit affects that of the before previous bit in the case of increasing the bitrate. Besides, increasing *BR* causes degradation of the eye-opening area because of the frequency bandwidth limitation of the mixer (f_{c2}).

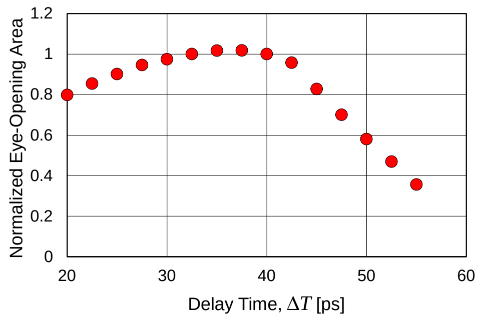

Fig. 12. Dependence of normalized eye-opening area upon delay time ΔT ($BR = 25$ Gb/s, $f_{\rm n} = 1$ GHz, $\beta_{\rm amp} = \pi/4$, $f_{\rm c1} = f_{\rm c2} = 20$ GHz).

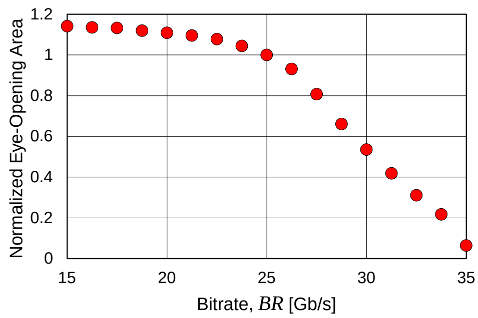

Fig. 13. Dependence of normalized eye-opening area upon bitrate BR ($\Delta T =$ 40 ps, $f_{\rm n} = 1$ GHz, $\beta_{\rm amp} = \pi/4$, $f_{\rm c1} = f_{\rm c2} = 20$ GHz).

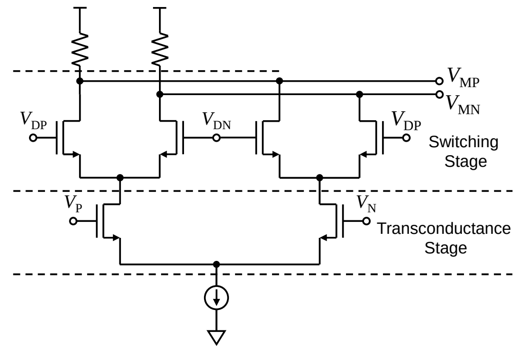

Fig. 14. Schematic diagram of standard Gilbert cell mixer.

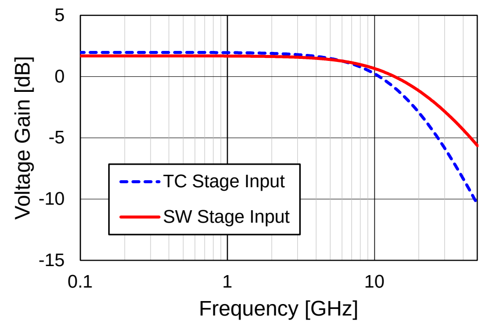

Fig. 15. Frequency response of designed Gilbert cell mixer in PLS.

IV. Evaluation of Designed Demodulation Circuit

A. Circuit description

Based on the above analyses, we designed a fully differential demodulation circuit (excluding TIAs and delay lines) for 25-Gb/s data transmission using the parameters of the 65-nm CMOS process. Fig. 14 shows a schematic diagram of a standard Gilbert cell mixer [12]–[14]. This mixer is a well-known circuit and has a fully differential configuration using two single-balanced switching mixers. For the delay detection, a differential signal is input to the transconductance (TC) stage, and the 1-bit delayed signal is input to the switching (SW) stage. The post-layout simulation (PLS) results of the frequency response of the designed mixer is shown in Fig. 15, where the solid and dashed lines mean the results for inputting the RF signal to the SW and TC stages and giving the DC bias to the TC and SW stages, respectively. The -3-dB frequency bandwidths in the case of the SW and TC stage inputs are 21 GHz and 14 GHz, respectively. Fig. 7 suggests that these values are sufficient for 25-Gb/s data transmission.

Fig. 16 shows a schematic diagram of a current-steering combiner. It consists of two current-mode logic (CML) differential amplifiers, and the load resistors are shared by the amplifiers. Assuming that the transconductance of NMOSs is $g_{\rm m}$ and the resistance of the load resistors is $R_{\rm L}$, the small-signal differential output $v_{\rm demd}$ can be expressed as

$$v_{\rm demd} = g_{\rm m} R_{\rm L} \left\{ (v_{\rm imp} - v_{\rm imn}) + (v_{\rm qmp} - v_{\rm qmn}) \right\}, \quad (24)$$

where $v_{\rm imp}$, $v_{\rm imn}$, $v_{\rm qmp}$, and $v_{\rm qmn}$ are small-signal input voltages of $V_{\rm IMP}$, $V_{\rm IMN}$, $V_{\rm QMP}$, and $V_{\rm QMN}$, respectively. Eq. (24) means that the output voltage is proportional to the sum of input voltages.

B. PLS results of designed demodulation circuit

We examined the operation of the designed demodulation circuit using Gilbert cell mixers and a current-steering combiner through post-layout simulations (PLSs). A layout of the designed demodulation circuit is shown in Fig. 17. The supplied voltage $V_{\rm DD}$ is set to 1.2 V. Based on Eqs. (16)–(19), differential input signals for the mixer, $V_{\rm IP/N}$, $V_{\rm QP/N}$, $V_{\rm IDP/N}$, and $V_{\rm QDP/N}$, are generated, where $\alpha(t)$ is a 25-Gb/s NRZ (PRBS $2^9 - 1$) signal with the amplitude from 0 to π. The voltage amplitude V' is set to 0.15 V, corresponding to a differential voltage of 0.6 $\rm V_{ppd}$. The offset voltage of 1.0 V is given to the input signals because the operating point (common-mode voltage) of the designed circuit was 1.0 V. The delay-time difference ΔT is set to 40 ps.

Fig. 18 shows eye diagrams of (a) the I-signal mixer output signal $V_{\rm IMP}$, (b) the Q-signal mixer output signal $V_{\rm QMP}$, and (c) the differential demodulation output signal $V_{\rm DEMP} - V_{\rm DEMN}$ in the designed demodulation circuit, where the phase-noise frequency and amplitude are $f_{\rm n} = 6$ GHz and $\beta_{\rm amp} = \pi/4$, respectively. In Figs. 18(a) and (b), the eye-opening is unclear due to the phase noise. On the other hand, a clear eye opening of the demodulation output can be observed in Fig. 18(c). Although low-frequency phase noise generated in adjacent bits can be cancelled out, the phase of high-frequency noise changes during 1-bit width and $\beta(t) \cong \beta(t - \Delta T)$ is not satisfied in Eq. (22). This is because the line width of the eye diagram in the case of $f_{\rm n} = 6$ GHz (167-ps period for the

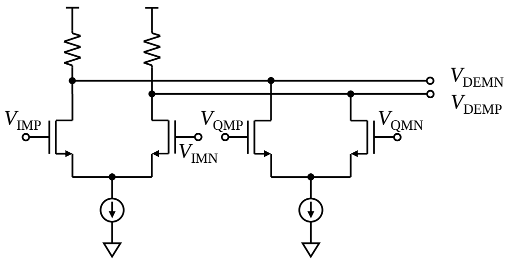

Fig. 16. Schematic diagram of current-steering combiner.

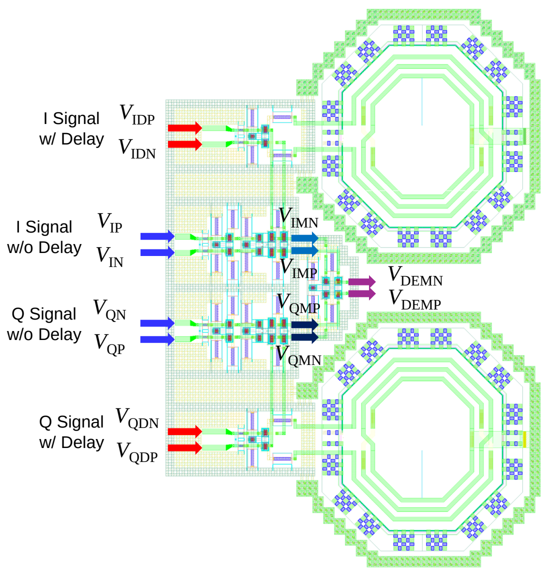

Fig. 17. Layout of designed demodulation circuit.

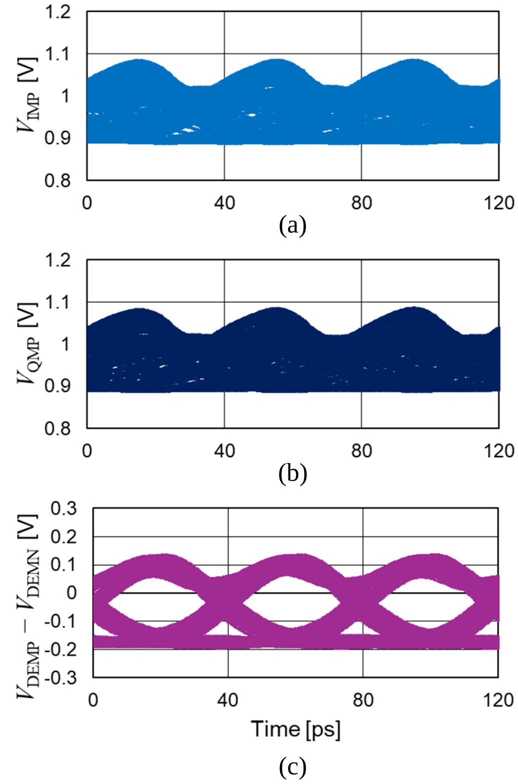

Fig. 18. PLS eye diagrams of (a) I-signal mixer output V_{IMP}, (b) Q-signal mixer output V_{QMP}, and (c) differential demodulation output $V_{\mathrm{DEMP}} - V_{\mathrm{DEMN}}$ in designed demodulation circuit ($BR = 25$ Gb/s, $\Delta T = 40$ ps, $\theta_{\mathrm{init}} = \pi/4$, $f_{\mathrm{n}} = 6$ GHz, $\beta_{\mathrm{amp}} = \pi/4$).

1-bit width of 40 ps) is broadened. According to CISPR 25, a standard for automotive applications, radiated noise in the frequency range of 150 kHz to 5.925 GHz must be considered. Therefore, our demodulation circuit is highly suitable for such applications.

V. Conclusions

We presented a method for canceling optical phase noise through differential detection using analog circuits. From the theoretical analyses considering the frequency bandwidth limitation of the analog circuits, the noise-canceling effect was verified, and the tolerance for operating conditions for noise canceling was clarified. Furthermore, the PLS results of the demodulation circuit using the parameters of the 65-nm CMOS process were shown, and its operation at 25 Gb/s was demonstrated.

References

[1] M. H. Ali *et al.*, "Simulative analyzing of covering suburban areas with 32 $\times$ 10 Gbps DWDM-PON FTTH using different dispersion and power," *Journal of Communications*, vol. 14, no. 5, pp. 381–389, 2019.

[2] J. Krause Perin *et al.*, "Data center links beyond 100Gbit/s per wavelength," *Optical Fiber Technology*, vol. 44, pp. 69–85, 2018, special Issue on Data Center Communications.

[3] T. Inoue *et al.*, "A 16-channel optical receiver circuit for a multicore fiber-based co-packaged optics module in a 65-nm CMOS chip," *IEEE Trans. Circuits Syst. II*, vol. 71, no. 5, pp. 2514–2518, 2024.

[4] K. Nagashima *et al.*, "An ultra-compact CPO transceiver based on a 1060-nm single-mode VCSEL array and multicore fibers," *J. Lightw. Technol.*, vol. 43, no. 13, pp. 6176–6186, 2025.

[5] T. Okoshi, "Recent advances in coherent optical fiber communication systems," *J. Lightw. Technol.*, vol. 5, no. 1, pp. 44–52, 1987.

[6] K. Kikuchi, "Fundamentals of coherent optical fiber communications," *J. Lightw. Technol.*, vol. 34, no. 1, pp. 157–179, 2016.

[7] T. Hirokawa *et al.*, "Analog coherent detection for energy efficient intra-data center links at 200 Gbps per wavelength," *J. Lightw. Technol.*, vol. 39, no. 2, pp. 520–531, 2021.

[8] K. Sheng *et al.*, "A 4.6pJ/b 200Gb/s analog DP-QPSK coherent optical receiver in 28nm CMOS," in *2022 IEEE International Solid-State Circuits Conference (ISSCC)*, vol. 65, 2022, pp. 282–284.

[9] L. Liu *et al.*, "DSP-free coherent receivers in frequency-synchronous optical networks for next-generation data center interconnects," *Advanced Photonics Nexus*, vol. 4, no. 3, p. 036013, 2025.

[10] A. Wissing *et al.*, "Analog coherent link with expanded link budget from integrated lasers and transmission through an O-band wavelength selective switch," *Opt. Express*, vol. 33, no. 24, pp. 50 656–50 665, Dec 2025.

[11] A. E. Abdelrahman *et al.*, "A 1.54-pJ/b 64-Gb/s 16-QAM intradyne coherent optical receiver in 28-nm CMOS," *IEEE J. Solid-State Circuits*, vol. 61, no. 1, pp. 20–32, 2026.

[12] B. Gilbert, "A precise four-quadrant multiplier with subnanosecond response," *IEEE J. Solid-State Circuits*, vol. 3, no. 4, pp. 365–373, 1968.

[13] M. O. Bekkaoui, "Gilbert cell mixer design in 65nm CMOS technology," in *2017 4th International Conference on Electrical and Electronic Engineering (ICEEE)*, 2017, pp. 67–72.

[14] I. Tanaka *et al.*, "A Gilbert cell mixer using cross-coupled capacitors for differential detection in 65-nm CMOS," in *2025 22nd International SoC Design Conference (ISOCC)*, 2025, pp. 1–2.